

INTAKE DESIGN EFFECTS ON INERTIAL PARTICLE SEPARATOR PERFORMANCE

Abdurrahman Burak Daldal, Gökhan Aslan* and Sinan Eyi***

**Turkish Aerospace*

06980 Ankara, Turkey

*** Middle East Technical University*

06800 Ankara, Turkey

Abstract

Inertial particle separator (IPS) is an engine integrated device to provide protection for foreign objects such as sand, dust etc. Due to the fact that IPS performance has a direct impact on the engine life, accurate estimation of separation efficiency becomes more important. When an engine is installed on a helicopter, it requires an intake system and aerodynamic characteristics of the incoming flow of the IPS changes significantly. In this study, intake effect on IPS performance is investigated with the most accurate method in the literature which uses unsteady approach and IDDES turbulence model. Results show that intake system increases the IPS separation performance.

1. Introduction

In many engineering applications, there are numerous undesirable objects known as ‘Foreign Object’ because of their dangerous effects. Dust, sand, stone, salt spray, bird, ice, snow and metal part are common examples of foreign object for air vehicles. Especially sand and dust are two of the foreign object sources, which are responsible from the erosion due to large number of dangerous operation areas. These areas create one of the most dangerous condition which is called as “brownout condition” for a helicopter. An example of a brownout condition is shown in Figure 1.



Figure 1: CH-53 helicopter in brownout condition. [1]

Brownout condition occurs during take-off, landing and hover in ground effect operations in dusty terrains. Helicopter rotor creates downwash, which interacts with the ground and causes dust clouds surrounding the helicopter. One of the most affected part of the helicopter due to these dust clouds is turbine engine. Air demand of the turbine engine is increased during the take-off and landing operations. Even at idle condition, where rotor downwash effect is minimum, dust contaminant still exists within the minimum required amount of air, which is delivered to the engine. As the engine is operating in the dust cloud, engine suction leads to ingestion of the sand/dust particles.

When a foreign object is ingested by a turbine engine, it encounters with the compressor section at first. For this reason, the most affected part of the engines is the first stage of compressor section [2]. Shape of the compressor blades can be deformed due to sand ingestion as presented in Figure 2.



Figure 2: Damaged compressor blades. [3]

There are several protection systems for helicopter engines and these systems are generally known as engine advanced protection systems (EAPS). Vortex tube systems, inlet barrier filters and inertial particle separators (IPS) are three well-known examples for EAPS. Vortex tube systems and inlet barrier filters are external equipment for helicopters; however, inertial particle separators are integrated in the turboshaft engine. In this paper, only IPS is investigated.

IPS is a device located at the frontmost of an engine which provides protection by deflecting both air and particle flows outward direction, where dust/sand particles, which have higher inertia, move into the scavenge duct and air, which has lower inertia, turns back to the core engine. Scavenge flow is derived with a fan; hence, some part of the incoming air evacuated with the particles. The ratio of the scavenge mass flow and incoming mass flow is defined as β and it is given in Eq. 1

$$\beta = \frac{\dot{m}_{\text{scavenge}}}{\dot{m}_{\text{scavenge}} + \dot{m}_{\text{core}}} \quad (1)$$

A simple representation of an IPS cross-section is illustrated in Figure 3.

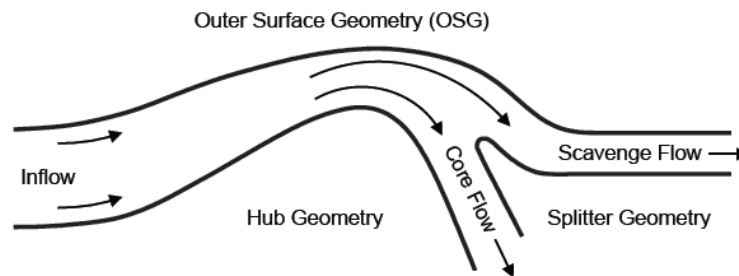


Figure 3: Inertial Particle Separator cross-section. [4]

When an engine is installed on a helicopter, a proper intake system is needed and it is designed by airframe manufacturer. Aerodynamics of the incoming flow into the engine varies according to the intake system design. In parallel with this variation, particle separation performance of the IPS is going to be different. The incoming air quality affected by intake design is measured by several parameters, which are pressure recovery, distortion and swirl. These parameters affect the IPS efficiency by changing the incoming flow properties. Swirl effect will be the main consideration of this study. Compressor rotation, helicopter attitudes (sideslip and pitch angle), rotor interactions and gust affect the swirl type (bulk, twin and offset swirl), angle, and direction in conjunction with the intake design. In the literature, all studies assume that the incoming flow to the IPS is uniform and straight; however, this is not true for installed engines.

Significant amount of experiments and computational studies have performed for both two and three-dimensional IPS geometries. Hamed et al. [5-7] studied 2-D T700 Engine IPS with steady without comparing any experimental data. Chen et al. [8] performed CFD analysis with 2-D axisymmetric annular IPS geometry with RANS approach. Only airflow is investigated in the CFD analyses and compared with the experimental data. Results show that CFD overestimates the velocity near wall and underestimates other regions.

Ghenaiet et al. [9], Taslim et al. [10, 11] studied 3-D annular IPS geometry and Jiang et al. [12] studied 3-D twisted IPS geometry with steady, RANS approaches and particle separation efficiency is investigated. However, there is not any experimental data to compare the results. Paoli and Wang [13] experimented 3-D fully annular IPS geometry; however, numerical study with the same geometry is also performed by using steady approach.

Connolly et al. [14-17] performed extensive study to obtain more accurate numerical model for IPS analysis. 3-D, unsteady CFD analysis for a planar IPS geometry is conducted for the first time by using Improved Delayed Detached Eddy Simulation (IDDES) turbulence model. Results show a good agreement with the experimental data for both flow-field and particle trajectories. In addition, Connolly studied scaling effects and axisymmetric effects on IPS performance with 2-D geometry by using RANS approach. It is stated that 2-D RANS simulations overestimate the separation efficiency.

The previous studies show that 2-D and 3-D RANS simulations incapable to capture the unsteady effects, which has a large impact on small particles. 3-D, unsteady analysis should be performed with a high fidelity turbulence model to obtain accurate separation efficiency results and flow-field calculations.

Despite of there are numerous studies about IPS, intake effects have not studied yet. In this study, IPS geometry is analysed with the unsteady approach and high fidelity turbulence model considering the intake effects. This study provides more realistic information for the engine life and deformation of the engine components. It is important to note that 3-D axisymmetric IPS geometry will be investigated for the first time with the most accurate method defined in the literature.

2. Methodology

As mentioned in the Introduction chapter, Barone and Connolly performed experiments with a planar IPS. A validation study is performed for both airflow and particle trajectory calculations by using these experimental results. The analyzed validation geometry and boundary conditions are given in Figure 4. Star-CCM+ software is used for CFD analyses.

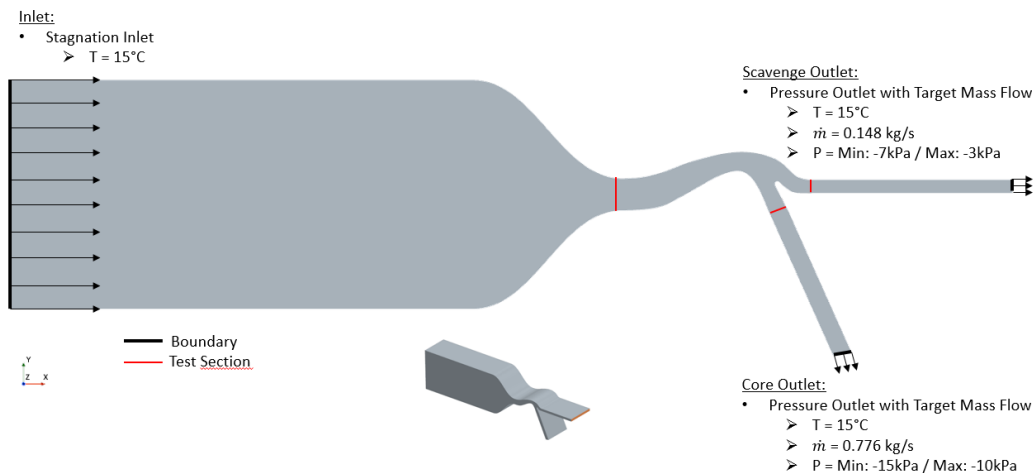


Figure 4: Validation geometry and boundary conditions [16]

The geometry shown in Figure 4 is used for CFD analysis, but there is a differences between original test and CFD geometry. Inlet and outlets are extruded in boundary normal direction to prevent pressure reflections at the boundaries. The boundary condition of the extruded walls are chosen as slip-wall. Inlet boundary condition is selected as stagnation inlet with zero Pascal gauge pressure. Core outlet and scavenge outlet boundaries are set as pressure outlet with target mass flow option. Pressure and mass flow rate values given in Figure 4 are implemented on these boundaries. Temperature is constant and 15°C at the all boundaries.

Fluid domain is discretized with unstructured polyhedral elements by using the same software. Regarding to the turbulence model, mesh is created by obeying the $y^+ < 1$ law. Mesh study is performed to visualize the solutions independency from the mesh size. Three different meshes are created with 4 million (coarse), 8 million (baseline) and 16 million (fine) elements. Both surface meshes and volume meshes at the mid-section are presented in Figure 5.

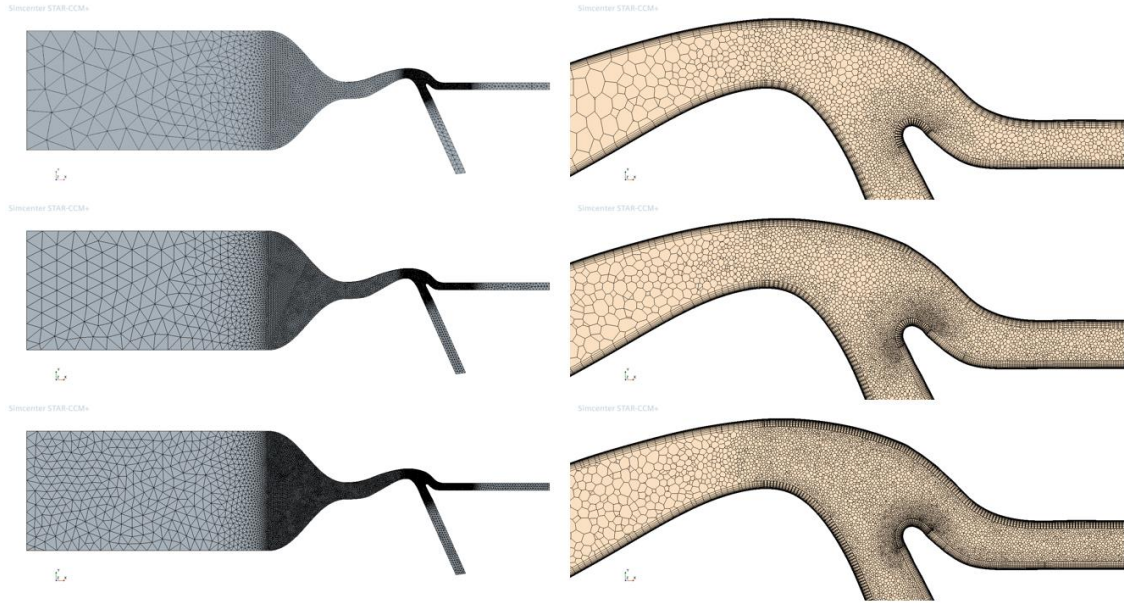


Figure 5: Surface mesh (left) and volume mesh at mid-plane (right).

According to the mesh study, since baseline and fine meshes have similar results, baseline mesh is used for flow and particle analysis. Detailed results of the mesh study will be presented in Result chapter.

In this study, analysis are accomplished in three parts which are:

- Steady flow analysis
- Unsteady flow analysis
- Unsteady flow analysis with particle injection

At the first part, analysis is started with the steady approach and it converged in 5000 iterations. Convergence is monitored by checking pressure and mass flow rate values at the core and scavenge outlet boundaries. Coupled implicit flow solver, which solves continuity and momentum conservation equations simultaneously, is used and these equations are presented in Eq. 2-4 by including the energy equation. [18] Fluxes are evaluated by using second order upwind discretization scheme. Air is used as material with ideal gas model.

$$\frac{\partial \rho}{\partial t} + \nabla \cdot (\rho \mathbf{V}) = 0 \quad (2)$$

$$\frac{\partial (\rho \mathbf{V})}{\partial t} + \nabla \cdot (\rho \mathbf{V} \times \mathbf{V}) = \nabla \cdot \boldsymbol{\sigma} + \mathbf{F}_b \quad (3)$$

$$\frac{\partial (\rho E)}{\partial t} + \nabla \cdot (\rho E \mathbf{V}) = \mathbf{F}_b \cdot \mathbf{V} + \nabla \cdot (\mathbf{V} \cdot \boldsymbol{\sigma}) - \nabla \cdot \mathbf{q} \quad (4)$$

where, ρ is density, \mathbf{V} is the velocity vector, $\boldsymbol{\sigma}$ is the stress tensor, \mathbf{F}_b is the body force per unit volume, E is the total energy per unit mass and \mathbf{q} is the heat flux vector. Stress tensor can also written as sum of normal and shear stresses.

$$\boldsymbol{\sigma} = -p\mathbf{I} + \mathbf{T} \quad (5)$$

where, p is the pressure, \mathbf{I} is the identity tensor and \mathbf{T} is the viscous stress tensor. Each flow variable, ϕ , (such as velocity, pressure etc.) have mean, $\bar{\phi}$, and fluctuating, ϕ' , components as shown in Eq.6.

$$\phi = \bar{\phi} + \phi' \quad (6)$$

Reynolds-Averaged Navier-Stokes equations can be re-written by using the only averaged term and additional modelling the fluctuating term of the flow variables as shown in Eq. 7-9.

$$\frac{\partial \rho}{\partial t} + \nabla \cdot (\rho \bar{\mathbf{V}}) = 0 \quad (7)$$

$$\frac{\partial(\rho \bar{\mathbf{V}})}{\partial t} + \nabla \cdot (\rho \bar{\mathbf{V}} \times \bar{\mathbf{V}}) = -\nabla \cdot \bar{p} \mathbf{I} + \nabla \cdot (\bar{\mathbf{T}} + \mathbf{T}_{RANS}) + \mathbf{F}_b \quad (8)$$

$$\frac{\partial(\rho \bar{E})}{\partial t} + \nabla \cdot (\rho \bar{E} \bar{\mathbf{V}}) = \nabla \cdot (\bar{\mathbf{T}} + \mathbf{T}_{RANS}) \bar{\mathbf{V}} + \mathbf{F}_b \bar{\mathbf{V}} - \nabla \cdot \bar{\mathbf{q}} - \nabla \cdot \bar{p} \bar{\mathbf{V}} \quad (9)$$

where, variables with overbar used for the mean value and one additional stress tensor T_{RANS} for the modelling of the fluctuating term is added. It is given in Eq.10.

$$\mathbf{T}_{RANS} = -\rho \begin{pmatrix} \overline{u'u'} & \overline{u'v'} & \overline{u'w'} \\ \overline{u'v'} & \overline{v'v'} & \overline{v'w'} \\ \overline{u'w'} & \overline{v'w'} & \overline{w'w'} \end{pmatrix} + \frac{2}{3} \rho k \mathbf{I} \quad (10)$$

where, k is the turbulent kinetic energy. These fluctuating terms are modeled in terms of mean flow variables and turbulent viscosity and it is known as Boussinesq approximation. It links the Reynolds stresses with the mean strain rate by using eddy viscosity.

$$\mathbf{T}_{RANS} = 2\mu_t \mathbf{S} - \frac{2}{3} (\mu_t \nabla \cdot \bar{\mathbf{V}}) \mathbf{I} \quad (11)$$

where, μ_t is the turbulent viscosity and S is the mean strain rate tensor.

In this study, turbulence is modeled by using $k-\omega$ SST turbulence model with low $y+$ approach and curvature correction option. In $k-\omega$ SST turbulence model, turbulent viscosity is modelled in terms of mean flow variables by solving additional transport equations for kinetic energy and specific dissipation rate.

At the second part, the time discretization is switched to unsteady approach. Time step is chosen as 5×10^{-6} seconds and 10 inner iterations which sufficient for continuity, three momentum and energy residuals to reach 1×10^{-4} . Additionally, the turbulence model is switched to the DES model. DES is a hybrid model that uses LES at the separated flow regions and it switches to RANS at the walls/boundary layers and irrotational regions. In LES turbulence model, a special filter is used to solve the Navier-Stokes (NS) equations. The flow variables have a filtered, $\tilde{\phi}$, and sub-filtered (or sub-grid), $\tilde{\phi}'$, components as shown in Eq.12.

$$\phi = \tilde{\phi} + \tilde{\phi}' \quad (12)$$

Navier-Stokes equations can be re-written by inserting the filtered and sub-filtered variables as shown in Eq. 13-15.

$$\frac{\partial \rho}{\partial t} + \nabla \cdot (\rho \tilde{\mathbf{V}}) = 0 \quad (13)$$

$$\frac{\partial(\rho \tilde{\mathbf{V}})}{\partial t} + \nabla \cdot (\rho \tilde{\mathbf{V}} \times \tilde{\mathbf{V}}) = -\nabla \cdot \tilde{p} \mathbf{I} + \nabla \cdot (\tilde{\mathbf{T}} + \mathbf{T}_{SGS}) + \mathbf{F}_b \quad (14)$$

$$\frac{\partial(\rho \tilde{E})}{\partial t} + \nabla \cdot (\rho \tilde{E} \tilde{\mathbf{V}}) = \nabla \cdot (\tilde{\mathbf{T}} + \mathbf{T}_{SGS}) \tilde{\mathbf{V}} + \mathbf{F}_b \tilde{\mathbf{V}} - \nabla \cdot \tilde{\mathbf{q}} - \nabla \cdot \tilde{p} \tilde{\mathbf{V}} \quad (15)$$

where, variables with over-tilde used for the filtered value and one additional stress tensor T_{SGS} for the modelling of the sub-grid scale stress term is added. It is given in Eq.16.

$$\mathbf{T}_{SGS} = 2\mu_t \mathbf{S} - \frac{2}{3} (\mu_t \nabla \cdot \tilde{\mathbf{V}}) \mathbf{I} \quad (16)$$

As LES requires very fine grid, solver may divert to RANS method due to coarse cells at the separation region. Moreover, if primis layer mesh is refined unnecessarily, solver may diverts from RANS to LES and results with artificial separation. While DDES method differs from DES by adding a delay factor, IDDES method differs from DES by adding dependence on the wall distance for sub-grid length scale to prevent this unrealistic phenomenon. In addition to those changes in models, flux-splitting scheme is switched to bounded-central, which is recommended for LES. This part of the analysis is continued until steady effects disappears which takes approximately 0.03 seconds.

At the last part of the analysis, Lagrangian Multiphase model is activated to analyze particle motion. One-way coupling, where particles are affected by fluid but do not have effects on the fluid flow, is used by assuming particles have

negligible impact on the airflow. Particles are modelled as solid glass sphere with constant 2500 kg/m³ density. Particle diameter is varied from 2µm to 200µm as defined in A4 Coarse Arizona test dust. [19] Pressure gradient force given in Eq.17 and drag force given in Eq.18 are the main forces acting on the particles.

$$\mathbf{F}_p = -V_p \nabla p_{static} \quad (17)$$

where V_p is the particle volume and ∇p_{static} is the gradient of the air static pressure.

$$\mathbf{F}_d = \frac{1}{2} C_d \rho A_p |\mathbf{v}_s| \mathbf{v}_s \quad (18)$$

where C_d is the drag coefficient, ρ is the air density, A_p is the projected particle area and v_s is the particle slip velocity. Drag coefficient can be estimated by using Schiller-Naumann correlation, which is suitable for spherical solid particles, and it is given in Eq.19.

$$C_d = \begin{cases} \frac{24}{Re_p} (1 + 0.15 Re_p^{0.687}) & Re_p \leq 10^3 \\ 0.44 & Re_p > 10^3 \end{cases} \quad (19)$$

where Re_p is defined as particle Reynolds number that is also defined in Eq.20.

$$Re_p = \frac{\rho |\mathbf{v}_s| D_p}{\mu} \quad (20)$$

where μ is defined as air dynamic viscosity, D_p is the particle diameter.

One of the main parameter affecting the particle motion is restitution coefficients. Particles leave the domain if they encounter the outlet boundaries and they bounce if they encounter with a wall boundary. Restitution coefficients define how particles move when they hit the wall boundary. A simple representation of a rebound event is shown in Figure 6

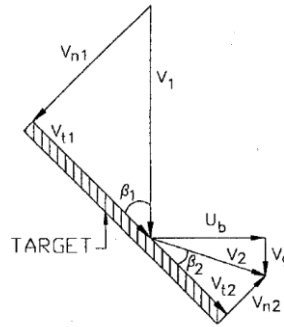


Figure 6: Rebound event [20]

There are two coefficients defined as normal and tangential restitution coefficients. Normal restitution coefficient is the ratio of the particle velocity after impact to particle velocity before impact in normal direction and tangential restitution coefficient is the same ratio in tangential direction. These coefficients are presented in Eq. 21-22.

$$e_n = \frac{V_{n2}}{V_{n1}} \quad (21)$$

$$e_t = \frac{V_{t2}}{V_{t1}} \quad (22)$$

There are several bounce model that are created with experimental results. Bounce model created by Tabakoff [20, 21], which is given in Eq. 23-24 is used in this study.

$$e_v = \frac{V_2}{V_1} = 0.65810 - 0.00877\beta_1 + 0.11954 \times 10^{-3} \beta_1^2 - 7.80954 \times 10^{-7} \beta_1^3 \quad (23)$$

$$e_{\beta} = \frac{\beta_2}{\beta_1} = 1.68634 - 0.06447\beta_1 + 1.35709 \times 10^{-3}\beta_1^2 - 8.70497 \times 10^{-7}\beta_1^3 \quad (24)$$

When all parameters in the model setup were arranged, particle analysis is started. Particles are released from the entrance of the test section shown in Figure 4 with zero initial velocity. Particles are added by using a line probe at the mid-section of the IPS. 10 particles are injected at each time step and particle injection is stopped after 0.006 seconds to reduce computational power. In total, 12 000 particles are injected. Analysis continued until particles leave the flow domain or they are stuck. Increasing the particle number to 40 000 and 120 000 does not affect the separation efficiency results. For each particle size, different analyses are conducted and separation efficiency results are obtained separately. These results are multiplied with a weighting factor [10] and final separation efficiency is calculated.

All the work up to here is used for planar IPS analysis. The same methodology will also be used for the investigation of intake effects. As mentioned in Chapter 1, only swirl effect is investigated at this study.

Swirl can be defined as flow angularity and it is one of the most common phenomenon observed at engine intakes after installation. Swirling flow at the intake may be generated due to several reasons or combination of them. Compressor rotation, intake type, aircraft attitude (angle of attack, sideslip angle etc.), gust and rotor interactions are the parameters affecting the swirl type and swirl angle. There are several swirl types such as bulk swirl, twin swirl and offset swirl. A simple representation of these swirl types are presented in Figure 8.

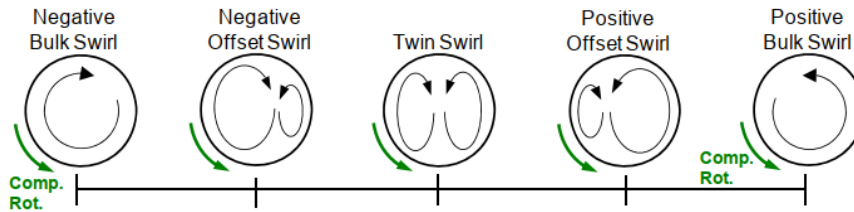


Figure 8: Swirl types [22]

If entire flow is rotating in one direction, it is called as bulk swirl. If flow is rotating in two opposite direction with the same magnitude, it is called as twin swirl. If flow is rotating in two opposite direction with different magnitude, it is called as offset swirl. Only bulk swirl will be investigated at this study for ease of modelling.

Swirl angle is defined as the invers tangent of the ratio of circumferential velocity to axial velocity. It is defined as positive if it is in the same direction with the compressor rotation. Swirl angle is given in Eq. 25 and illustrated in Figure 9.

$$\alpha = \tan^{-1} \left(\frac{U_{\theta}}{U_x} \right) \quad (25)$$

Figure 9: Swirl angle [22]

Since planar geometry is not suitable for swirling flow investigation, an annular IPS geometry is needed. A new annular IPS geometry is obtained by revolving the 2-D geometry around the axis of the engine center, where engine radius is 0.5m. The new geometry is created by using Siemens NX software with an effort maintaining the flow field characteristics. For this purpose, core to scavenge area ratio is preserved with the original test geometry. When preserving the area ratio, some necessary geometry modifications such as directing the core leg to the axial direction are accomplished. When core leg is directed in both axial and vertical directions (as in validation geometry), core flow outlet gets closer to the rotation center. Hence, area of the core outlet becomes smaller than the scavenge outlet, where it is vice versa at the original geometry, at the end of the revolving operation. Moreover, in real engines core leg stands in axial direction. At last, intake geometry is simplified and hub, splitter and OSG geometries remain the same.

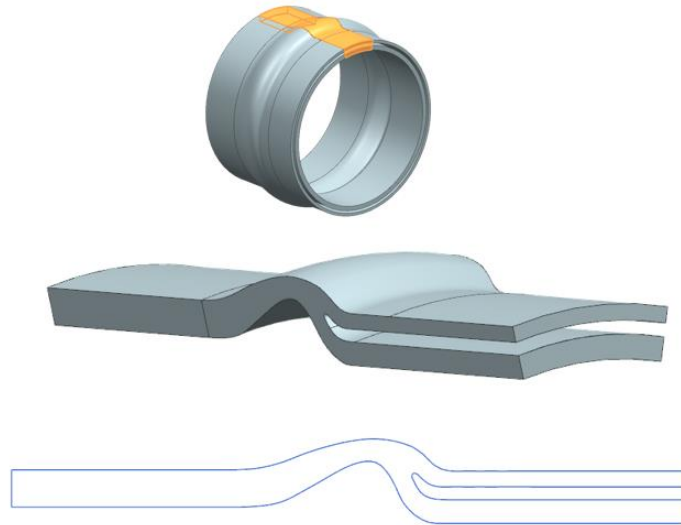


Figure 10: Annular IPS geometry, 24° slice and 2-D cross-section.

CFD analysis are performed with 24° slice of the annular IPS geometry, which is given in Figure 10, to reduce the mesh size and computational time. Periodic boundary condition is applied at the sidewalls of the IPS. Target mass flow rate values at the core and scavenge outlet boundaries are set as 0.818kg/s and 0.156kg/s respectively for 16% scavenge flow ratio case. The same pressure intervals are used for minimum and maximum values. A reference frame is defined to model the swirling flow and it is applied at the inlet boundary. Swirl angle is chosen as 15° regarding the auxiliary power unit (APU) side intake example in [22].

Baseline mesh configuration is used for meshing the annular IPS geometry and new mesh study is not performed. Both surface and volume meshes are presented in Figure 11.

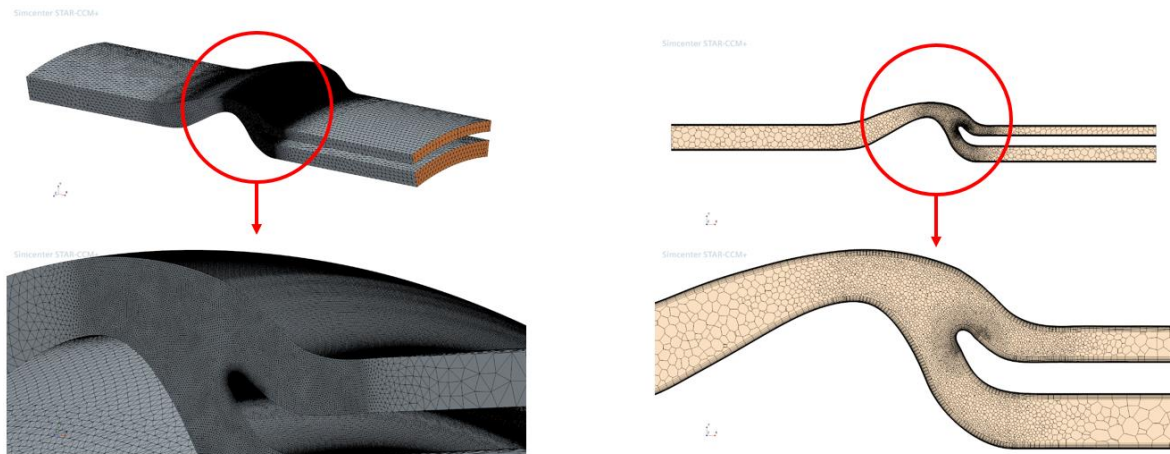


Figure 11: Annular IPS surface mesh (left) and volume mesh (right).

In order to make a correct comparison, the new geometry is solved without swirling incoming flow at the beginning. Then, swirling flow is analyzed at the same conditions. The three steps mentioned at the beginning of this chapter are used to obtain flow field and separation efficiency results.

3. Results

3.1. Validation – Planar IPS Analysis

As mentioned previously, a mesh study is performed with three different mesh size (4, 8 and 16 million cell elements) and their results are compared. Analyses for all grids are run with 16% scavenge flow ratio condition.

PIV data is used to compare velocity profiles at core and scavenge channels around splitter. Axial velocity (V_x) is measured for scavenge flow at $x=20\text{cm}$ plane and vertical velocity (V_y) is measured for core flow at $y=4.8\text{cm}$ plane.

Measurement locations for both core and scavenge channels are also illustrated in Figure 13. Velocity profiles are plotted according to the planes given in Figure 12 for different times and presented in the same figure.

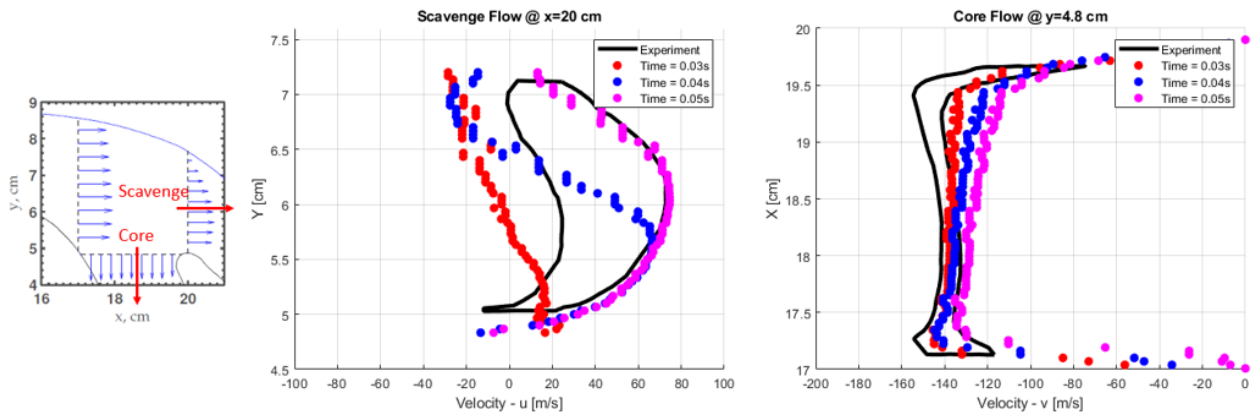


Figure 12: Velocity measurement locations and velocity profiles at these locations [23, 24]

As it can be seen from Figure 12, velocity profiles changes dramatically in time for both scavenge and core flows. Since velocity profile oscillates due to unsteady characteristics of the flow, an envelope is obtained with the time dependent data. Core and Scavenge velocity profile envelopes and their comparison with the experimental data [23, 24] are shown in Figure 13.

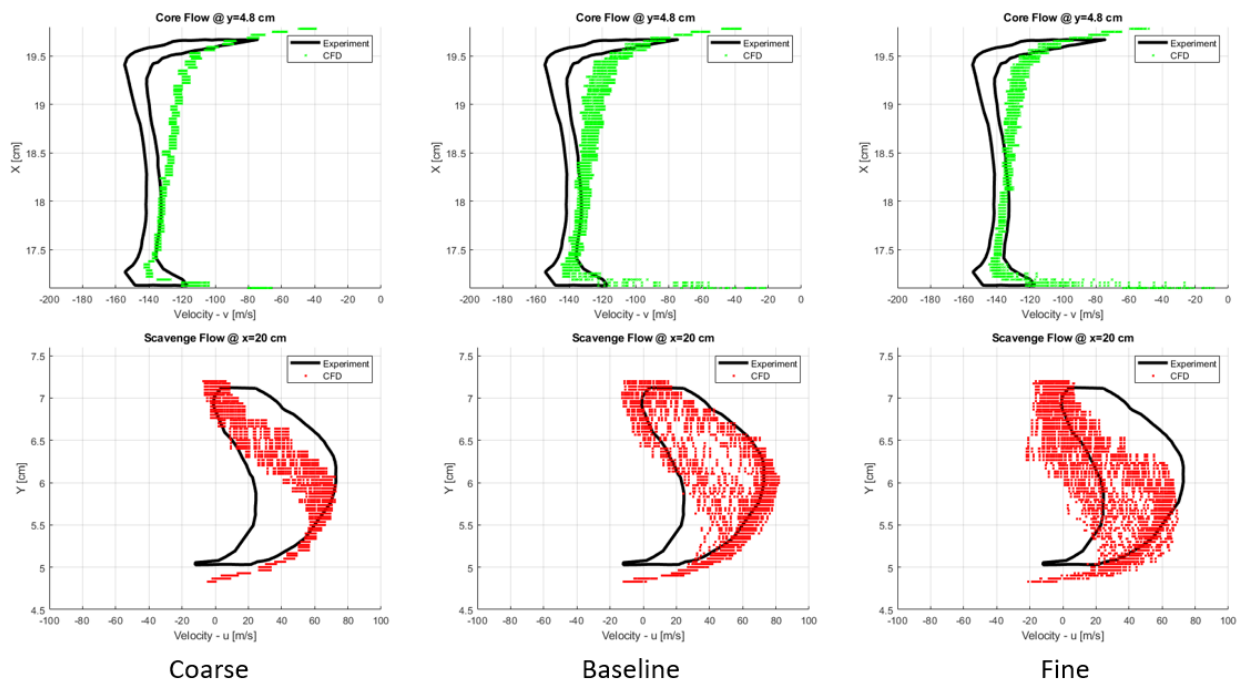


Figure 13: Velocity measurement comparison for different grids.

As it can be seen from Figure 13, none of the results match with the experimental flow-field around splitter (lower-left side of the scavenge flow envelope and upper-right side of the core flow envelope) due to lack of experimental data which cannot be obtained regarding the laser reflections around the wall. In addition, coarse grid oscillates in a smaller envelope than the experimental envelope. It cannot solve most of the regions in scavenge & core flow envelopes correctly. Baseline and fine grid provide similar results and their results' sweep many regions in the experimental envelope except upper-left side of the core flow envelope. Hence, further studies will be performed with baseline grid.

Moreover, velocity contours around splitter region from CFD analysis (left) are compared with the experimental data (right) in Figure 14.

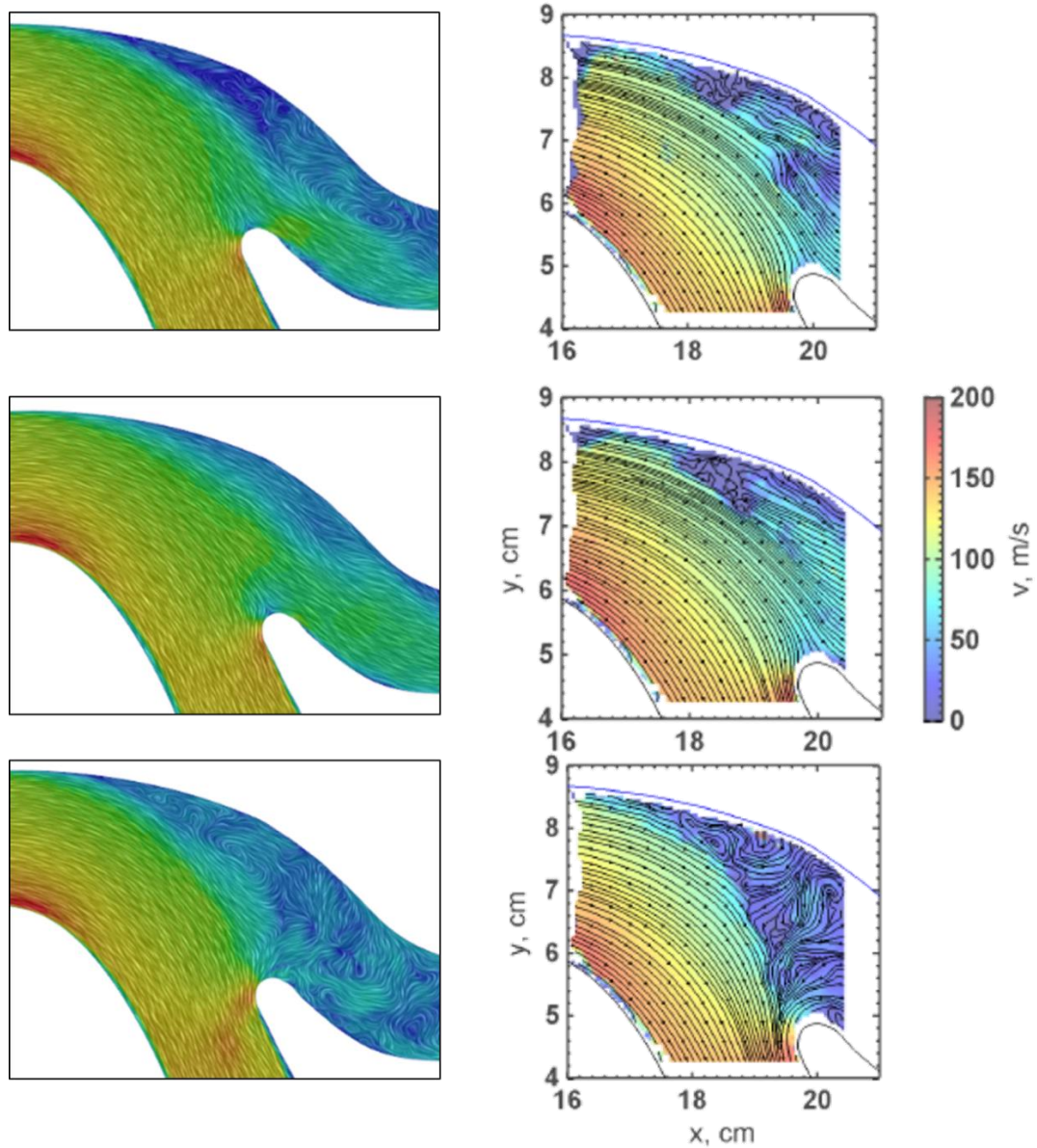


Figure 14: Flow-field around splitter at different time steps. CFD result (left) comparison with experimental data (right) [25].

As it can be seen from Figure 14, velocity contours around splitter are presented at three different time. At each time, flow behave differently. At the top, scavange flow is partially blocked due to separation on the OSG. At the middle, separation is disappeared and scavange channel is open. At the bottom, scavange flow is completely blocked due to huge vortices in the scavange channel and flow is directed to core channel. These three flow phase occur periodically in the IPS.

At the same time, flow-fields of experiment and CFD results with baseline grid are compared in order to make sure the CFD model is appropriate. Oil streak visualizations on the core side of the OSG are compared with the CFD results in Figure 15. [4]

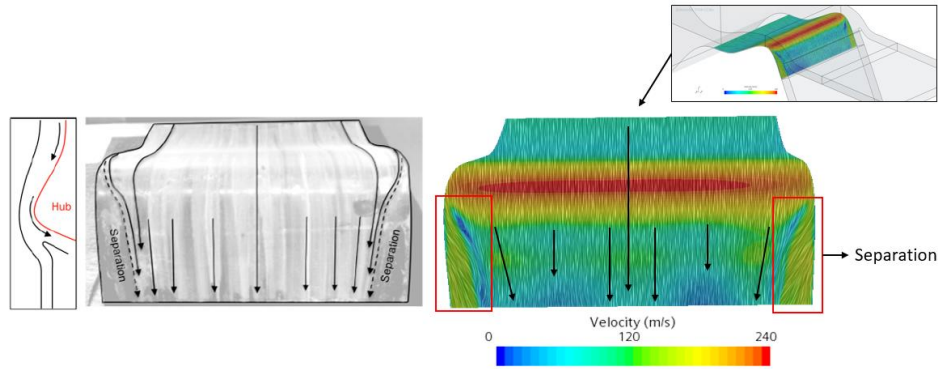


Figure 15: Velocity contour on core side of the OSG. CFD result comparison with experimental oil streak.

According to Figure 15, very similar velocity fields are obtained at the CFD results with the experimental oil streak visualization. The same separations, which are marked with red rectangles, can be seen at the sidewalls on the core side of the OSG.

In general, CFD results have a good agreement with the experimental data in terms of flow-field comparison. Particle analysis is also performed with A4 Coarse test dust for 10%, 16% and 20% scavenge flow ratio. Figure 16 shows separation efficiency results with experimental comparison.

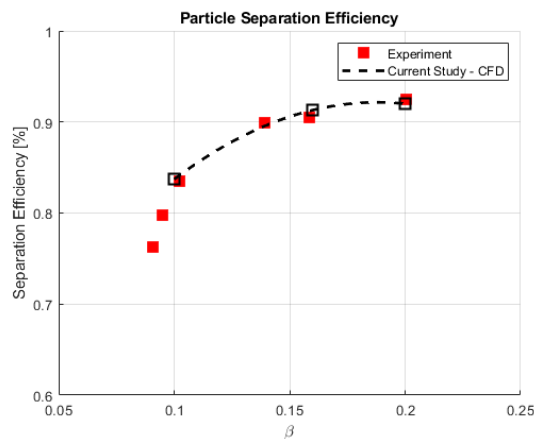


Figure 16: Particle separation efficiency for A4 Coarse test dust with different scavenge flow ratio.

According to the Figure 16, it is clear to see that particle separation results match with the experimental results perfectly. Error is found less than 1% for each condition. The method used for particle motion prediction is validated and further studies can be performed with this method.

3.2. Annular IPS Analysis

Annular IPS is analyzed with both straight and swirling flow condition to observe the intake effect on separation efficiency more clearly. Before separation efficiency results, flow-field is investigated. Comparison between straight and swirling flows is hard with a two dimensional plane visualization; hence, flow-fields are visualized in 3-D with streamlines. Streamlines (plotted when the massive flow separation is occurred) of both core and scavenge flows are presented separately in Figure 17 for straight flow condition.

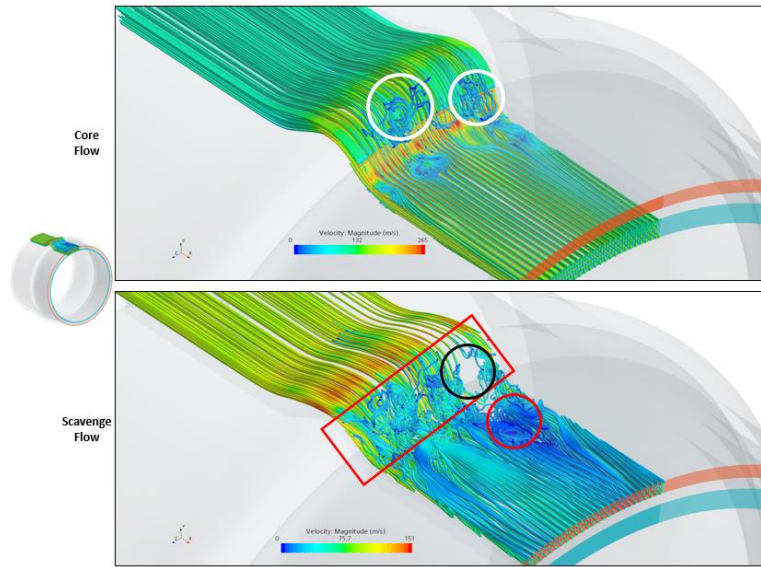


Figure 17: Streamlines for straight flow.

As it can be seen from Figure 17, recirculation regions around OSG, marked with red rectangle and red circle, can be seen easily in the scavenge flow streamlines. In addition, a re-ingestion event is observed in the core flow. Some part of the scavenge flow, marked with white circles, rotated back to the core flow which will also cause re-ingestion of the particulate matter into the engine. Moreover, an empty region (low-pressure region), marked with black circle, is occurred due to this event and a huge circulation in the scavenge flow, marked with red circle, is appeared regarding the high-pressure to low-pressure movement tendency of the flow.

Streamlines of both core and scavenge flows are presented separately in Figure 18 for swirling flow condition.

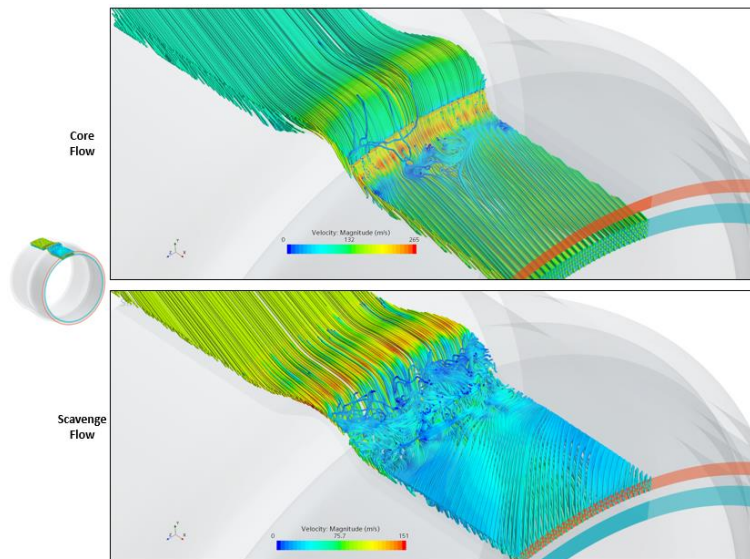


Figure 18: Streamlines for swirling flow.

It can be seen that from Figure 19, swirling flow boundary is implemented successfully. As swirling angle is reduced in the core flow after the bifurcation part, flow has higher swirl angle in the scavenge flow. This phenomenon is occurred due to the boundary condition implementation. Flow direction of the core and scavenge flow outlet boundaries are implemented with the boundary normal option. Because of this implementation, swirl angle in the core flow is reduced due to its higher inertia however, swirl angle in the scavenge flow is increased to conserve the angular momentum. Moreover, re-ingestion event is disappeared in the swirling flow condition. This is probably due to the

less inertia in the longitudinal direction of the core flow where some amount of its longitudinal inertia transferred to the lateral direction to swirl the flow.

After the flow-field investigations, particle trajectories and particle flow are analyzed. Particle trajectories and particle velocity are illustrated in Figure 19 for $2\mu\text{m}$, $10\mu\text{m}$ and $20\mu\text{m}$ particles.

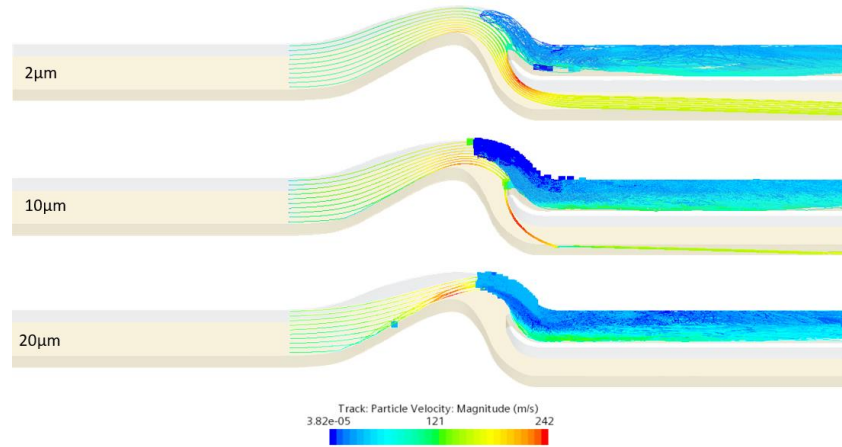


Figure 19: Particle trajectories and particle velocity for swirling flow.

As it can be seen from Figure 19, particle separation efficiency increases as particle size increases which is an expected phenomenon. The bigger particles have higher inertia and they tend to follow the ballistic trajectory. However, the smaller particles have less inertia and they tend to follow the streamline trajectory. One of the other reason for the particle ingestion is recirculation region on the OSG. When the scavenge side is clogged due to the huge recirculation and flow separation, particles with diameter less than $10\mu\text{m}$, $St < 1$ where particles tend to follow streamline trajectories, get into the recirculation region and re-ingested by the core flow. Sometimes these particles do not get into the recirculation and just interacts with the splitter. An example of the re-ingested $10\mu\text{m}$ particles is presented in Figure 20.

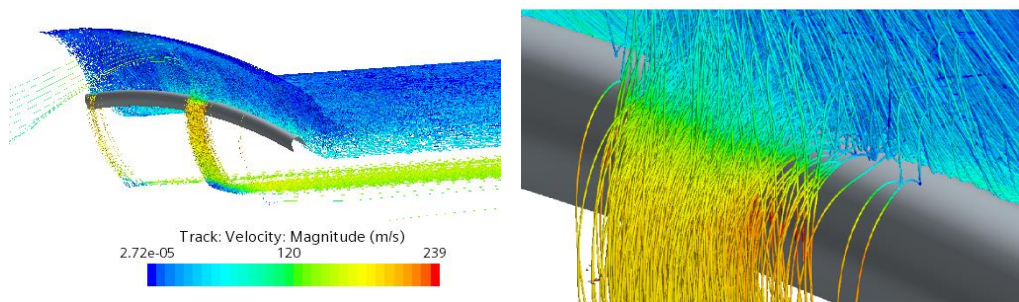


Figure 20: $10\mu\text{m}$ particle trajectories and splitter interaction.

As presented in Figure 20, many particles interact with the splitter due to the blocked scavenge channel and move to the core channel. A similar re-ingestion case is also shown in Connolly's study. [16] However, some particles can be captured by circulation region in the scavenge channel and they stuck in the separated zone. Their speed may reach near zero until the separation disappear. Moreover, particle separation efficiency of the each particle size is presented in Figure 21 for both straight and swirling flow.

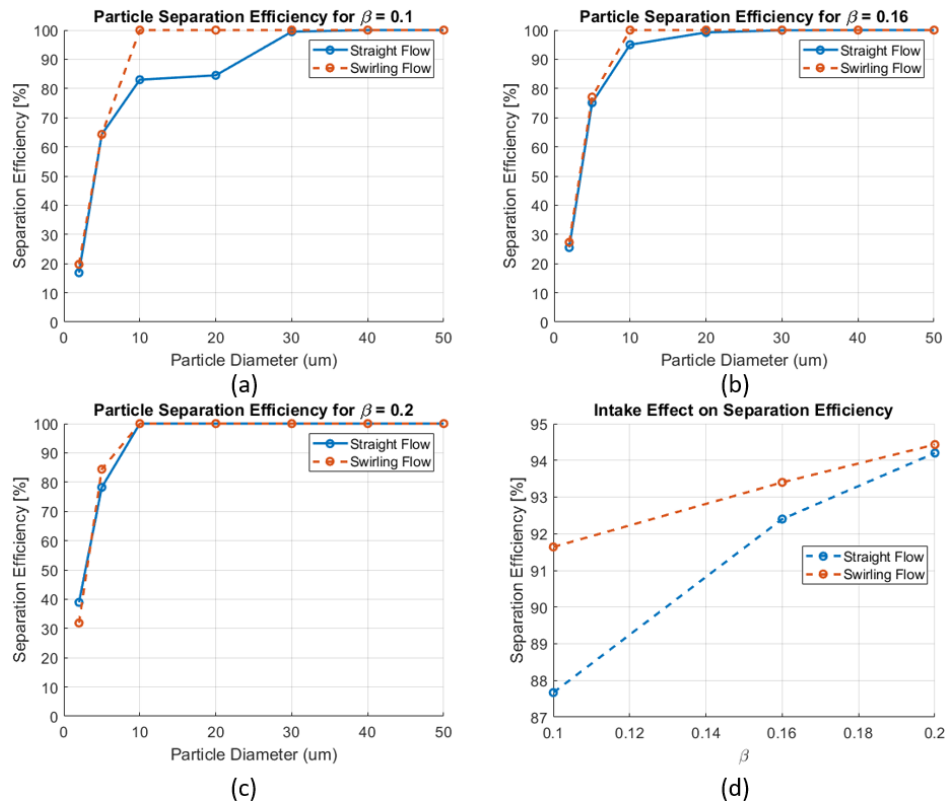


Figure 21: Separation efficiency comparison of each particle for both straight and swirling flow for $\beta=0.1$ (a), $\beta=0.16$ (b), $\beta=0.2$ (c). Cumulative separation efficiency (d).

According to Figure 21.a-c, it is easy to say that swirl affects the separation efficiency in a positive way. Separation efficiency of the all particles is higher when the flow swirls except $2\mu\text{m}$ particles with $\beta=0.2$ condition. Adding a swirl effect to the flow increases the centrifugal force acting on the particle. However, linear momentum of the flow and particle reduces at the same time. When increased centrifugal force leads the particle to be scavenged, reduced particle momentum leads the particle to be affected by bounce forces more than drag forces and results with ingestion by the core flow. There is a balance at this point.

According to Figure 21.d, as β increases, the difference between the separation efficiencies of straight and swirling flow decreases. When $\beta=0.1$, the highest difference between the separation efficiencies is observed which is approximately 4%. When $\beta=0.2$, the difference between the separation efficiencies reduces to approximately 0.2%. In addition, separation efficiency of the particles larger than $30\mu\text{m}$ have not affected by the flow where separation efficiency of the particles with high inertia is dominated by the bouncing forces.

4. Conclusion

In this study, one of the intake effects, swirl effect, on the IPS separation performance is investigated with CFD. 3-D unsteady analyses are performed with a high fidelity turbulence model due to incapability of the RANS methods to capture the entire physical phenomenon. Particle motion is estimated with the Lagrangian approach. At the beginning, the computational models for flow-field and particle motion are validated with the experiment, which performed with a planar IPS geometry. A new IPS geometry is created to implement the swirling flow, which requires annular geometry. When creating the new IPS geometry, a special study is paid attention to preserve the flow-field characteristics. The new geometry is analyzed with the straight flow and then the swirling flow. Results show that swirling flow increase the separation efficiency approximately 4% when $\beta=0.1$ and 0.2% when $\beta=0.2$. If separation efficiency of the IPS increases from 85% to 92%, engine life increases 10 times. [26] Maintenance and inspection intervals of the several engine sections depend on the IPS efficiency. Keeping the time between inspections/maintenance operations shorter brings loss of time, supplies and money. However, keeping it longer may results with loss of equipment or even loss of aircraft.

References

- [1] Head E., What it's like flying the CH-53K helicopter into a brownout. Vertical Mag. (n.d.). Retrieved December 12, 2021, from <https://verticalmag.com/news/flying-ch-53k-helicopter-into-brownout>.
- [2] J. P. V. D. Van Der Walt and A. Nurick, Erosion of dust-filtered helicopter turbine engines part i: Basic theoretical considerations, *Journal of Aircraft*, vol. 32, pp. 106–111, Jan. 1995.
- [3] Witek, L., Bednarz, A., & Stachowicz, F. 2015. Fatigue analysis of compressor blade with simulated foreign object damage. *Engineering Failure Analysis*, 58, 229–237.
- [4] Barone, D., Loth, E., & Snyder, P. 2012. A 2-D inertial particle separator research facility. 28th Aerodynamic Measurement Technology, Ground Testing, and Flight Testing Conference.
- [5] Hamed, A. 1982. Particle dynamics of inlet flowfields with swirling vanes. *Journal of Aircraft*, 19(9), 707–712.
- [6] Tabakoff, W., & Hamed, A. 1984. Installed engine performance in dust-laden atmosphere. *Aircraft Design Systems and Operations Meeting*.
- [7] Hamed, A., Jun, Y., & Yeuan, J. 1993. Particle dynamics simulations in inlet separator with an experimentally based bounce model. 29th Joint Propulsion Conference and Exhibit.
- [8] Chen, H., Tan, H.-jun, Yuan, Y.-qing, Du, M.-chen, & Xie, M.-xiang. 2017. Separated flows in bifurcated region of a vaneless inertial particle separator. *Journal of Aircraft*, 54(3), 1234–1237.
- [9] Ghenaiet, A., & Tan, S. C. 2004. Numerical study of an inlet particle separator. Volume 2: Turbo Expo 2004.
- [10] Taslim, M. E., Khanicheh, A., & Spring, S. 2009. A numerical study of sand separation applicable to engine inlet particle separator systems. *Journal of the American Helicopter Society*, 54(4), 042001.
- [11] Taslim, M. E., & Spring, S. 2010. A numerical study of sand particle distribution, density, and shape effects on the scavenge efficiency of engine inlet particle separator systems. *Journal of the American Helicopter Society*, 55(2), 22006–220069.
- [12] Jiang, L. Y., Benner, M., & Bird, J. 2012. Assessment of scavenge efficiency for a helicopter particle separation system. *Journal of the American Helicopter Society*, 57(2), 41–48.
- [13] Paoli, F., & Wang, T. 2011. Numerical Study of internal flow field and flow passage improvement of an inlet particle separator. *Frontiers in Energy*.
- [14] Connolly, B. J. 2016. A Parametric Study of Inertial Particle Separator Geometry. [Master's thesis, University of Virginia].
- [15] Connolly, B. J., Loth, E., & Smth, C. F. 2019. Unsteady simulation of an inertial particle separator. *AIAA Propulsion and Energy 2019 Forum*.
- [16] Connolly, B. J. 2020. Inertial Particle Separators Experiments, Simulations, and Design Insights. [Doctoral dissertation, University of Virginia].
- [17] Goss, C. M., Connolly, B. J., Loth, E., & Smth, C. F. 2019. Scaling effects on inertial particle separator performance. *AIAA Propulsion and Energy 2019 Forum*.
- [18] Siemens Industries Digital Software. 2021. Simcenter STAR-CCM+ User Guide, version 2021.3. *Turbulence*.
- [19] ISO 12103-1. 2016. Road Vehicles -- Test Contaminants for Filter Evaluation -- Part 1: Arizona Test Dust
- [20] Tabakoff, W., Murugan, D., & Hamed, A. 1994. Effect of target materials on the particle restitution characteristics for turbomachinery application. 32nd Aerospace Sciences Meeting and Exhibit.

- [21] Tabakoff, W., Malak, M., & Hamed, A. 1985. Laser measurements of solid particles rebound parameters impacting on 2024 aluminum and 6A1-4V titanium alloys. 18th Fluid Dynamics and Plasmadynamics and Lasers Conference.
- [22] SAE AIR5686. 2022. A Methodology for Assessing Inlet Swirl Distortion.
- [23] Barone, D. L., Loth, E., & Snyder, P. H. 2014. Fluid dynamics of an inertial particle separator. 52nd Aerospace Sciences Meeting.
- [24] Connolly, B. J., Loth, E., & Frederic Smith, C. 2022. Unsteady separated flows in an S-duct and a bifurcating duct. *Journal of Aircraft*, 59(1), 47–57.
- [25] Snyder, P. H., Barone, D., & Loth, E. 2015. Unsteady flow dynamics within an inertial particle separator. Volume 1: Aircraft Engine; Fans and Blowers; Marine.
- [26] Potts, J. T. 1990. Why an engine air particle separator (EAPS)? Volume 2: Aircraft Engine; Marine; Microturbines and Small Turbomachinery.
- [27] Duffy, R. J., & Shattuck, B. F. 1975. Integral engine inlet particle separator. volume 1. technology program.
- [28] Duffy, R. J., & Shattuck, B. F. 1975. Integral engine inlet particle separator. volume 2. design guide.
- [29] Barone, D. 2014. Inertial Particle Separator Multiphase Dynamics. [Doctoral dissertation, University of Virginia].
- [30] Chen, N., Du, J., Hu, Y., Ji, H., & Yuan, Y. 2020. Study of the flow and impingement of water droplets inside an inertial particle separator. *AIP Advances*, 10(4), 045313.